

FUEL CELLS

Covalent organic framework–based porous ionomers for high-performance fuel cells

Qingnuan Zhang¹, Shuda Dong¹, Pengpeng Shao¹, Yuhao Zhu¹, Zhenjie Mu¹, Dafei Sheng¹, Teng Zhang¹, Xin Jiang², Ruiwen Shao³, Zhixin Ren¹, Jing Xie¹, Xiao Feng^{1*}, Bo Wang^{1*}

Lowering platinum (Pt) loadings without sacrificing power density and durability in fuel cells is highly desired yet challenging because of the high mass transport resistance near the catalyst surfaces. We tailored the three-phase microenvironment by optimizing the ionomer by incorporating ionic covalent organic framework (COF) nanosheets into Nafion. The mesoporous apertures of 2.8 to 4.1 nanometers and appendant sulfonate groups enabled the proton transfer and promoted oxygen permeation. The mass activity of Pt and the peak power density of the fuel cell with Pt/Vulcan (0.07 mg of Pt per square centimeter in the cathode) both reached 1.6 times those values without the COF. This strategy was applied to catalyst layers with various Pt loadings and different commercial catalysts.

The oxygen reduction reaction (ORR) at the cathode in commercial proton-exchange membrane fuel cells (PEMFCs) is catalyzed by precious metals, which are usually platinum (Pt)-based materials. Reducing the Pt loading of PEMFCs while maintaining high power density and durability is still challenging (1–3). Although new catalysts have been prepared through alloying and nanostructuring strategies (4), their performance is often evaluated by the rotating disk electrode (RDE) technique and is hard to translate into a membrane electrode. In a catalyst layer (CL) of the membrane electrode assembly (MEA), the ORR happens at oxygen-water-catalyst

three-phase interfaces. To react, oxygen must pass across a few-nanometer-sized ionomer component and encounters substantial mass transport resistance. Thus, optimizing the three-phase microenvironment becomes crucial to maximize the activity of the catalyst in PEMFCs.

Ionomers, which are the proton-conducting link between the proton-exchange membrane and Pt catalyst sites for the proton current flow, dominate the three-phase microenvironment in PEMFCs. Currently, perfluorosulfonic acid polymer (PFSA, or Nafion) is the most widely used ionomer (5, 6). However, PFSA is inevitably tightly coated on the catalyst, which causes high gas diffusion resistance (7). The diffusion

resistance from the ionomer and water accounts for 80% of total gas resistance, and the remainder mainly originates from secondary pores, which refer to the pores >20 nm that exist between aggregates of agglomerates (7). Moreover, the $-\text{SO}_3\text{H}$ groups in Nafion can strongly adsorb and occupy active sites on the Pt surface, which can decrease the Pt activity and thus reduce corresponding mass activity (MA) and power density (8, 9).

Several approaches have been used to solve these problems. Efforts have been devoted to optimizing the ionomers or carbon supports. Embedding Pt in the channel of the carbon support could avoid direct interaction between Pt and the ionomer (9, 10). The carbon supports can be tuned to adjust the ionomer coverage on their surface (11). Altering the side chain of the ionomers (12–15) can reduce the $-\text{SO}_3\text{H}$ inhibition effect. The incorporation of additives such as hydrophobic polytetrafluoroethylene (16, 17) or pore-forming materials (18–20) can

¹Beijing Key Laboratory of Photoelectronic/Electrophotonic Conversion Materials, Key Laboratory of Cluster Science, Ministry of Education, Frontiers Science Center for High Energy Material, Advanced Technology Research Institute (Jinan), School of Chemistry and Chemical Engineering, Beijing Institute of Technology, Beijing 100081, P. R. China. ²Orthopaedics Department, China-Japan Friendship Hospital, Beijing 100081, P. R. China. ³Beijing Advanced Innovation Center for Intelligent Robots and Systems, School of Medical Technology, Beijing Institute of Technology, Beijing 100081, P. R. China.

*Corresponding author. Email: bowang@bit.edu.cn (B.W.); fengxiao86@bit.edu.cn (X.F.)

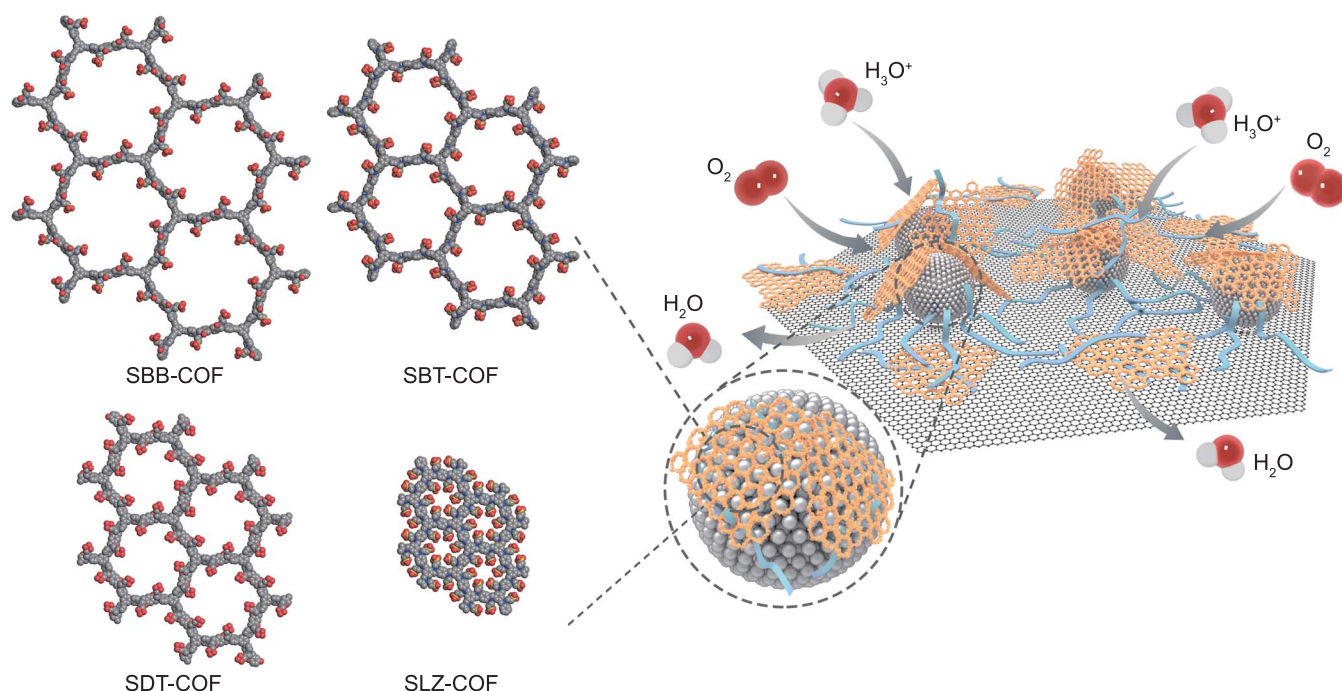


Fig. 1. Overview of Pt/C@COF-Nafion. Schematic illustration of the gas and proton transfer in Pt/C@COF-Nafion. Structure models of SLZ-COF, SDT-COF, SBT-COF, and SBB-COF with aperture sizes of 1.2, 2.8, 3.6, and 4.1 nm, respectively, are shown. Red, O; blue, N; gray, C; and yellow, S. Hydrogen is omitted for clarity.

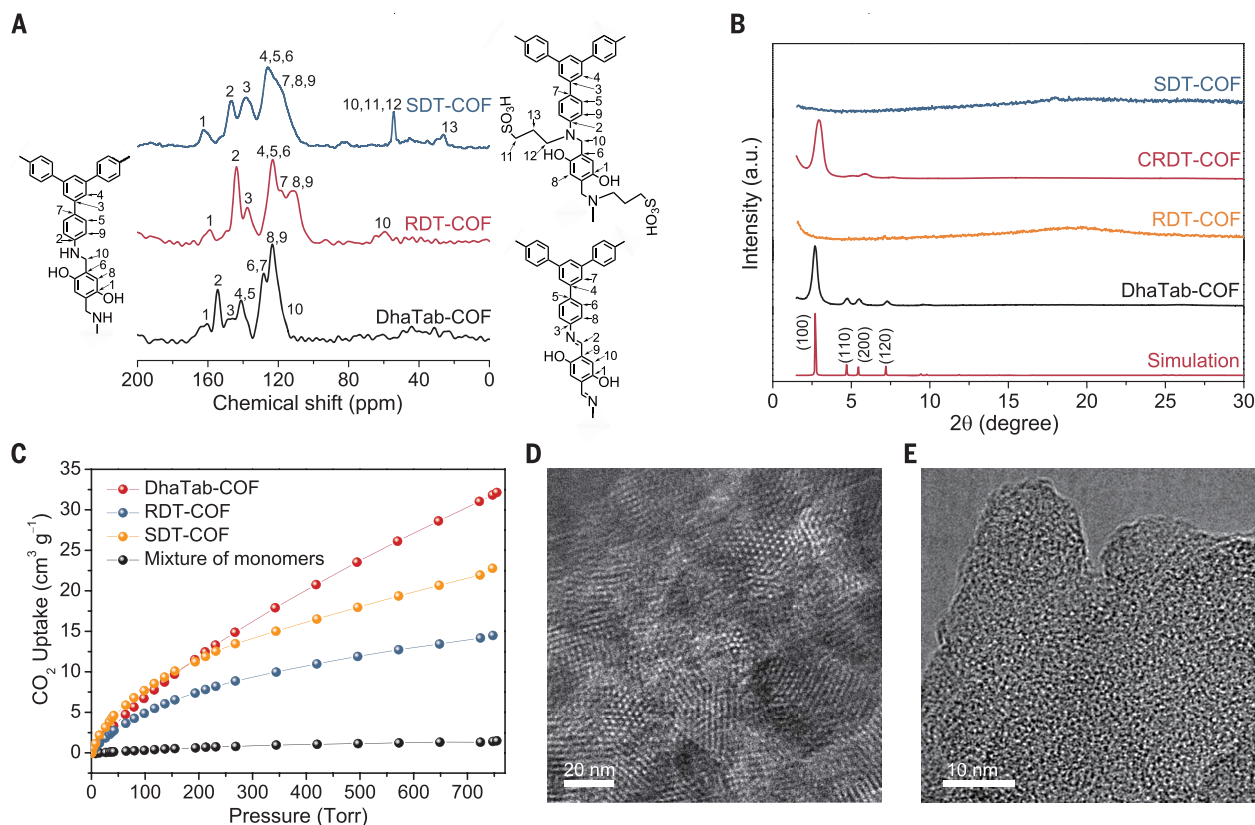


Fig. 2. Structural characterizations of SDT-COF. (A) ^{13}C ssNMR spectra of SDT-COF, RDT-COF, and DhaTab-COF. (B) Experimental PXR patterns of SDT-COF, CRDT-COF, RDT-COF, and DhaTab-COF and the simulated PXR pattern of DhaTab-COF (AA stacking). (C) CO_2 sorption isotherm profiles of DhaTab-COF, RDT-COF, SDT-COF, and the mixture of monomers. (D and E) HR-TEM images of (D) DhaTab-COF and (E) SDT-COF.

improve mass transfer. Nevertheless, it remains a substantial challenge to optimize gas diffusion without sacrificing proton conductivity in the CL to achieve highly efficient fuel cells with low Pt loading. Covalent organic frameworks (COFs), which are an emerging class of crystalline porous polymers that are constructed by topological linking organic building units, show notable potential in mass transfer given their atomically pre-designable structure, high surface area, and ease of precise modification (21–23). They have been proposed as proton-exchange membranes in the forms of pressed pellets or assembled membranes (24, 25) for the PEMFCs. However, their mechanical performances, as well as the H_2 crossover risk from anode to cathode in the fuel cell, present obstacles for their practical application.

Here, we fabricated high-performance fuel cells with commercial Pt/C (Pt/Vulcan) by incorporating a sulfonic acid functionalized DhaTab-COF (SDT-COF) into Nafion as a composite ionomer (the corresponding CL is denoted as Pt/C@SDT-Nafion) (Fig. 1). The SDT-COF has inherent hexagonal nanopores partitioned by molecular building units, which impart the CL with improved gas transport capability. The $-\text{SO}_3\text{H}$ group linking to the pore walls ensures

the rapid proton conduction within the channels, whereas Nafion helps reduce interface impedance between the COF nanosheets. The rigidity and high porosity of SDT-COF also help weaken adsorption of the $-\text{SO}_3\text{H}$ group on Pt. The particular properties of this COF were demonstrated by performing control experiments with other COFs with different pore sizes (Fig. 1) as well as other rigid sulfonated materials. The addition of COFs with mesoporous apertures in the CL promoted ORR at the three-phase interface and improved Pt use to realize high power density for PEMFCs with low Pt loading.

Synthesis and characterizations of SDT-COF

We synthesized DhaTab-COF from its monomers, 2,5-dihydroxyterephthalaldehyde (Dha) and 1,3,5-tris(4-aminophenyl)benzene (Tab), which are linked by imine bonds. This crystalline COF has periodic and unidirectional columnar arrays of 3.4-nm hexagonal channels. Further reduction of its imine linkages to secondary amine linkages afforded reduced DhaTab-COF (RDT-COF) (figs. S1 to S3) to ensure its acid stability for fuel cell application (26–28). We then obtained SDT-COF by grafting propanesulfonic acid sodium salt to the pore walls of RDT-COF, followed by acidification.

Their chemical compositions and structures were confirmed with the elemental analyses (supplementary materials), Fourier-transform infrared (FTIR) spectra (fig. S4 and table S1), the ^{13}C cross-polarization magic-angle spinning (CP-MAS) solid-state nuclear magnetic resonance (ssNMR) spectra (Fig. 2A), x-ray photoelectron spectroscopy (XPS) (figs. S5 and S6), powder x-ray diffractions (PXRDs) (Fig. 2B), and N_2 sorption isotherms (fig. S7).

Compared with DhaTab-COF, the crystallinity and the Brunauer-Emmett-Teller (BET) surface area of RDT-COF were greatly reduced, which we attributed to the conformational flexibility of the secondary amine linkages (fig. S2) (29). The retention of the extended framework linked by covalent bonding of RDT-COF was further confirmed by successfully converting it to crystalline and porous cyclic carbamate-linked COF (CRDT-COF) (Fig. 2B and figs. S8 to S10) (29). In the high-resolution transmission electron microscopy (HR-TEM) images, ordered mesopores and disordered pores can be observed in the DhaTab-COF and SDT-COF, respectively (Fig. 2, D and E). The RDT-COF and SDT-COF both showed CO_2 uptake ability (273 K) (Fig. 2C), whereas the physical mixture of the monomers did not show apparent adsorption. These results demonstrated that the

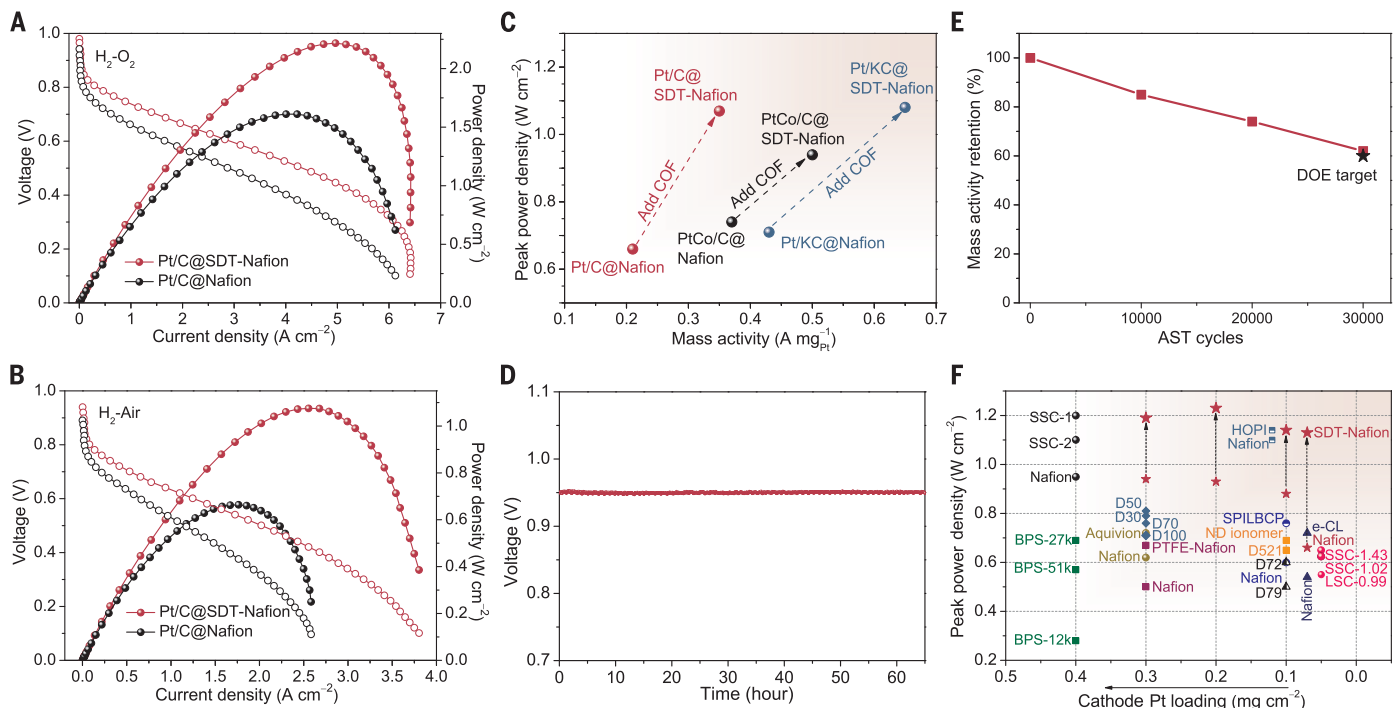


Fig. 3. Fuel cell performance and durability. (A) H_2 - O_2 and (B) H_2 -air fuel cell I - V polarization (without iR compensation; i , current; R , resistance) and power density plots of the cells with Pt/C@Nafion and Pt/C@SDT-Nafion measured at 80°C and 100% RH under 150 kPa abs. (C) Comparison of the MAs and peak power densities of MEAs evaluated under H_2 -air conditions. (D) OCV test of the MEA with Pt/C@SDT-Nafion at 90°C lasted 65 hours. (E) Attenuation of the MA of Pt/C@SDT-Nafion in the

AST with 30,000 cycles. (F) Comparing the cathode Pt loading and peak power density for MEAs based on commercial Pt/C catalyst in this study and previous reports (table S3). Smaller red stars indicate Pt/C@Nafion data; larger red stars are the Pt/C@SDT-Nafion data. BPS, sulfonated poly(arylene ether sulfone); HOPI, high oxygen permeability ionomer; ND, nanodispersion PFSA; PTFE, polytetrafluoroethylene; SPILBCP, sulfonated poly(ionic liquid) block copolymer; SSC, short-side-chain PFSA.

polymeric layers of RDT-COF and SDT-COF can still create nanosized apertures that allow gas permeation. The grafting fraction of sulfonic acid groups based on the elemental analysis was 60%. Thermogravimetric analysis (TGA) showed that the decomposition temperature of SDT-COF was 200°C (fig. S11).

After grafting, the SDT-COF could be dispersed in water and exhibited a Tyndall effect (fig. S12). The atomic force microscope also showed that SDT-COF adopted a nanosheet morphology with an average thickness of ~0.8 nm (fig. S13). The ion exchange capacity (IEC) of SDT-COF is 1.85 mequiv g^{-1} as calculated by means of elemental analysis and 1.70 mequiv g^{-1} as calculated by titrating with NaOH solution to a phenolphthalein end point, which is greater than that of the commercial Nafion DE2020 ionomer (1.03 to 1.12 mequiv g^{-1}). The temperature dependence of the proton conductivity was measured at 100% relative humidity (RH) (figs. S14 to S16), and the conductivity of the pressed SDT-COF tablet was 95.3 mS cm^{-1} . The proton transport property of Nafion DE2020 and SDT-COF/Nafion (ratio 1:1) thin films was also investigated by using gold interdigitated electrodes, and the result showed that the proton conductivities were increased slightly after adding SDT-COF (fig S17).

Fuel cell performance and durability

For PEMFC measurements, the ratio of total ionomer to carbon (I/C) was set at 0.8 (30). We then optimized the component proportions of SDT-COF and Nafion in the ionomer by using H_2 - O_2 single-cell tests (5.0 cm^2 MEAs). Among the CLs that have been evaluated (fig. S18), including pure Pt/C, Pt/C@Nafion, Pt/C@SDT, and Pt/C@SDT-Nafion (mass ratio of SDT-COF and Nafion = 1:2, 1:1, or 2:1), Pt/C@SDT-Nafion (mass ratio = 1:1) had the largest current density and power density. After optimization, the Pt loadings were fixed at 0.07 and 0.05 $mg_{Pt} cm^{-2}$ in the cathode and anode CLs, respectively.

The current-voltage (I - V) polarization and power density distributions of Pt/C@Nafion and Pt/C@SDT-Nafion fuel cells are shown in Fig. 3A, measured under 150 kPa absolute pressure (abs) (50 kPa back pressure) fully humidified O_2 . The peak power density of Pt/C@SDT-Nafion fuel cell achieved 2.21 $W cm^{-2}$, which was 1.4 times of the controlled MEA without SDT-COF. Pt/C@SDT-Nafion exhibited an MA of 0.35 $A mg_{Pt}^{-1}$ in the H_2 - O_2 test versus 0.21 $A mg_{Pt}^{-1}$ for Pt/C@Nafion (Fig. 3C). The electrochemical active surface area (31) of Pt/C@SDT-Nafion (67.4 $m^2 g_{Pt}^{-1}$) was also higher than that of the Pt/C@Nafion (41.4 $m^2 g_{Pt}^{-1}$) (fig. S19 and table S2). A similar

trend was observed under the H_2 -air condition. Under the 150 kPa abs fully humidified air condition, the PEMFC with Pt/C@SDT-Nafion reached a peak power density of 1.08 $W cm^{-2}$, which was 1.6 times of the Nafion-based MEA. At 0.7 V, the power density was 2.4 times greater than the value without SDT-COF (Fig. 3B). The peak power density and limiting current densities reported here exceed those reported for other low Pt-loading cathodes ($\leq 0.1 mg_{Pt} cm^{-2}$) obtained with commercial Pt/C (Fig. 3F and table S3). These results showed that the SDT-COF in the CL enabled the exposure of more active sites of Pt.

The accelerated stress tests (ASTs) were conducted according to the US Department of Energy (DOE) catalyst stability evaluation protocols (figs. S20 to S22). After 30,000 cycles, the MA decreased by 38%, which meets the requirement of the DOE 2025 technical target of 40% (Fig. 3E) (32). The open circuit voltage (OCV) was maintained at 90°C for 65 hours, which also shows the electrochemical stability of SDT-COF (Fig. 3D). Because peroxide by-product is the main source of the attack on the CL (3), the chemical stability of SDT-COF was further proved by soaking it in 1% hydrogen peroxide for 5 hours; no degradation was observed, as evidenced by the IR spectra (fig. S23).

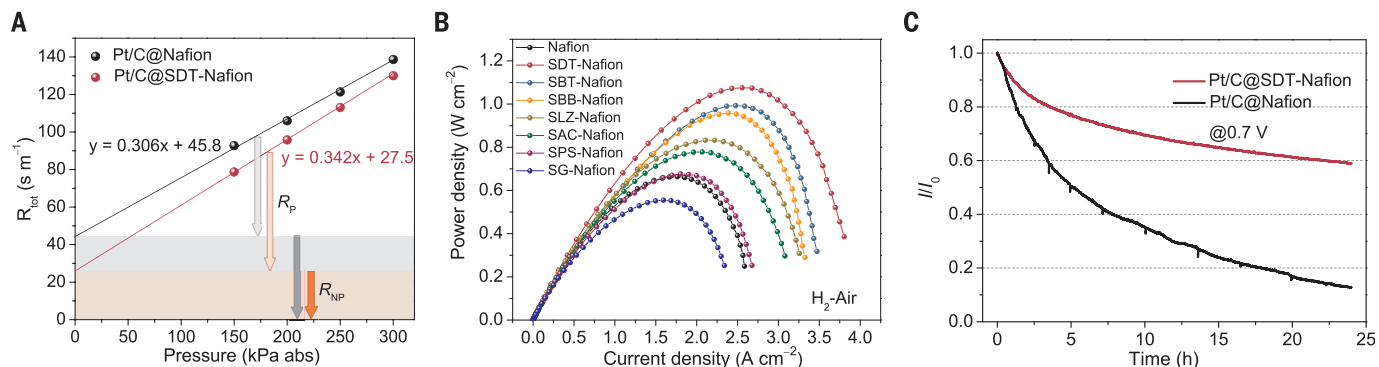


Fig. 4. Mass transport. (A) R_{tot} of Pt/C@Nafion and Pt/C@SDT-Nafion plotted versus the absolute pressure. (B) Comparison of the power density of MEAs with different ionomers in CLs under H_2 -air condition. (C) Twenty-four-hour continuous working tests for Pt/C@SDT-Nafion and Pt/C@Nafion without water management.

In addition, to meet different MEA requirements for various practical fuel cell stacks, we tested the MEA performance with cathode to anode loadings of $0.1/0.1\ mg_{Pt}\ cm^{-2}$, $0.2/0.2\ mg_{Pt}\ cm^{-2}$, and $0.3/0.3\ mg_{Pt}\ cm^{-2}$, respectively (figs. S24 to S28). The power densities were all improved after the addition of SDT-COF, irrespective of the Pt loadings (Fig. 3F). To further demonstrate the applicability of this strategy, we evaluated the PEMFC performance by using commercial PtCo/C and Pt/Ketjenblack (Pt/KB) catalysts with the addition of SDT-COF/Nafion composite ionomer (Fig. 3C and figs. S29 to S31). The parameter improvements of the PEMFC performance by using our porous ionomer design strategy are summarized in table S2. The MA of PtCo/C and Pt/KB catalysts in MEA with SDT-COF reached $0.50\ A\ mg_{Pt}^{-1}$ and $0.65\ A\ mg_{Pt}^{-1}$, respectively, which surpassed the DOE 2025 technical target ($0.44\ A\ mg_{Pt}^{-1}$).

Mechanism discussions

The ORR performance in the CL depends on the O_2 transfer resistance, proton accessibility, and RH. The mass transfer resistance of O_2 in the H_2 -air cell is calculated based on the limiting current density (fig. S32). (17, 33). The apparent value obtained is the total mass transport resistance (R_{tot}), which includes pressure-dependent resistance (R_p) and pressure-independent resistance (R_{NP}). Flow field channels and the gas diffusion layer govern the R_p , whereas the Knudsen mass transport and the resistance derived from the Pt-ionomer-water interface dominate the mass transport resistance of R_{NP} (10). The slope and intercept in Fig. 4A indicate the O_2 diffusion resistances R_p and R_{NP} , respectively. The R_{NP} were 45.8 and $27.5\ s\ m^{-1}$ for the Pt/C@Nafion and Pt/C@SDT-Nafion, respectively, which reflects the positive effect of SDT-COF on gas diffusion.

Electrochemical impedance spectroscopy (EIS) can also be used to assess the individual contributions of the transport and kinetic processes to the PEMFCs (figs. S33 and S34). The EIS data were fitted to a modified Randles cell

equivalent circuit model (table S4) to monitor the ohmic resistance (R_{ohm}), polarization resistances (Z_{ct} , Z_{ox} , Z_{mass}), and capacitances (C_1 , CPE1, and CPE2) (34). The total mass transfer resistance of O_2 was reduced after adding SDT-COF for both the H_2 - O_2 cell (from 0.027 to 0.0068 ohms) and the H_2 -air cell (from 0.055 to 0.032 ohms).

To further investigate the relation between COF structure and CL performance, we prepared COFs with the same topology but different aperture sizes, which included sulfonated LZU-1 (SLZ-COF), sulfonated DbdTab-COF (SBT-COF), and sulfonated DbdBtt-COF (SBB-COF) with aperture sizes of 1.2, 3.6, and 4.1 nm, respectively (Fig. 1 and figs. S35 to S44). Furthermore, sulfonated graphene (SG) (nonporous), sulfonated activated carbon (SAC) (pore size: 0.9 nm), and sulfonated polystyrene spheres (SPSs) (nonporous) were also used as the controls. SPSs and SG both increased the heterogeneity of the interface yet did not improve MEA performance (Fig. 4B and figs. S45 to S48). Even for the sulfonated porous structure with micropores such as SAC and SLZ-COF, only slight performance improvements were observed.

By contrast, SDT-COF, SBT-COF, and SBB-COF with aperture sizes of 2.8, 3.6, and 4.1 nm, respectively, could boost the power density of the fuel cells (Fig. 4B and figs. S49 to S52), which indicates that the intrinsic mesopores of the frameworks were critical for promoting oxygen permeation. We also measured O_2 gas transport with additive-Nafion mixed membranes, in which the ratio of additive/Nafion was set as 2:8 to ensure the compactness and integrity of the resultant membrane. Oxygen permeability was directly related to the pore structure of these additives (figs. S53 to S56 and table S5). In addition, we tested the O_2 permeability of Nafion membrane and SDT-COF-Nafion membrane under 100% RH. The O_2 permeability of SDT-COF/Nafion (2:8) under the humid condition had a permeability of 36 Barrer, whereas that of Nafion decreased to 0 Barrer.

To further exclude the influence of secondary large pores (fig. S57) on the cell performance, we measured gas sorption isotherms and deduced the corresponding pore size distributions of the Pt/C@additive-Nafion (fig. S58). The results showed that only the addition of COF led to the exposure of the mesopores in the Pt/C, revealing that the gas molecules could reach the catalyst through the apertures in the COF framework. The interface heterogeneity induced by other rigid-structured nanomaterials (SG and SPSs) could not improve gas permeation to the catalyst surface, whereas Nafion blocked the mesopores of Pt/C. These results showed that only the COF-Nafion membrane allowed relatively rapid gas permeation, whereas the Nafion membranes with nonporous additives did not boost the permeation of gas molecules. As for PEMFCs, both proton conductivity and O_2 gas transport ability together affect cell performance. Because the proton conductivity did not markedly increase after adding SDT-COF, the O_2 gas transport ability dominated the performance.

The dry proton accessibility to the Pt sites increased from 0.61 to 0.76 after adding SDT-COF (fig. S59) (9). We then performed 24-hour continuous H_2 -air fuel cell tests under 0.7 V constant voltage without scheduled refreshing (Fig. 4C and fig. S60). The currents dropped 41 and 87% for Pt/C@SDT-Nafion and Pt/C@Nafion, respectively, which indicates that the porous ionomer improved resistance to flooding. We measured the static and dynamic water vapor sorptions (figs. S61 to S63). Compared with Nafion, the water desorption of SDT-COF exhibited obvious hysteresis phenomena. We also conducted the fuel cell measurements under 30% RH and 60% RH conditions. Along with reducing RH, the decreasing degree of the cell performance was reduced after adding SDT-COF (fig. S64). Thus, SDT-COF facilitated the mass transfer with or without accumulated water.

The RDE measurement could reveal the inhibitory effect of ionomer on a Pt surface and the mass transfer resistance between the Pt

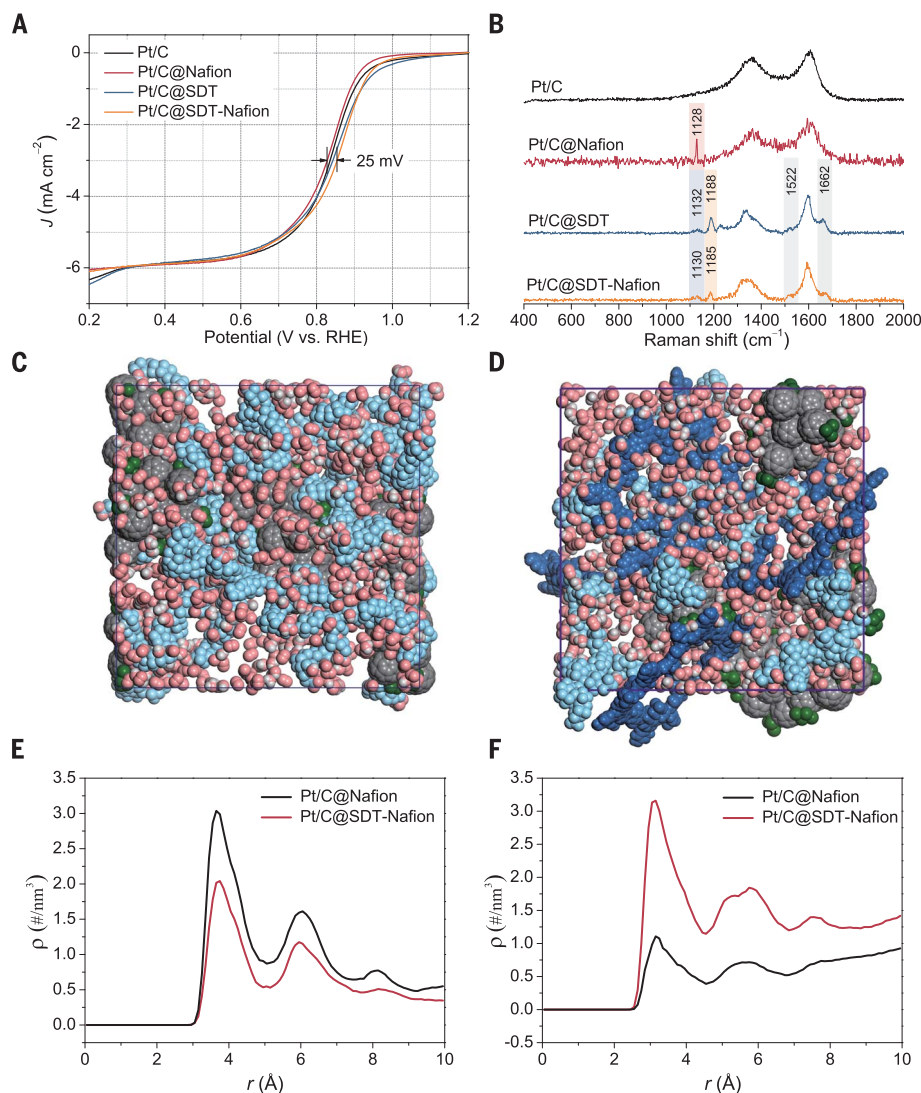


Fig. 5. Poisoning effect. (A) LSV and (B) Raman spectra of Pt/C catalysts with different ionomers. RHE, reversible hydrogen electrode. (C and D) Molecular models of the multicomponent CL with Nafion (C) and the combination of SDT-COF and Nafion (D). Light blue, Nafion; dark blue, SDT-COF; green, Pt; pink, O; white, H; gray, C. (E and F) Comparison of the atom density profiles of (E) Pt-S and (F) Pt-O (O from O₂).

particles and ionomer. As shown in the linear sweep voltammetry (LSV) curves (Fig. 5A), the halfwave potential increased in the order of Pt/C@Nafion < Pt/C ≤ Pt/C@SDT < Pt/C@SDT-Nafion. This result suggested that SDT-COF could weaken the Nafion inhibition. The XPS analysis showed that -SO₃H groups did not change the valence state of Pt but could strongly adsorb onto Pt and occupy the active sites (figs. S65 and S66). In the Raman spectrum of Pt/C@Nafion, the peak at 1128 cm⁻¹ was caused by the adsorption of sulfonic acid groups on the surface of Pt atoms [$\delta(\text{Pt-SO}_3)$] (9, 35). In comparison, the peak assigned to $\delta(\text{Pt-SO}_3)$ was greatly weakened for Pt/C@SDT-Nafion (Fig. 5B and figs. S67 and S68). The rigid framework structure of SDT-COF helped decrease the interaction of flexible sulfonic acid groups to Pt, which was beneficial to

improving the MA of the catalysts. The peaks at 1132 and 1188 cm⁻¹ represented the stretching vibration of the sulfonic acid group, and both peaks had a slight red shift when SDT-COF was mixed with Nafion. The Raman spectra of physically mixed pure Pt nanoparticles with SDT-COF (fig. S69) also showed that the sulfonic acid groups located in the pores of the rigid COF framework could avoid direct contact with the Pt particles.

We performed TEM, energy dispersive x-ray spectroscopy (EDS) mapping (figs. S70 to S73), and three-dimensional TEM (movies S1 and S2) and found uniform wrapping of SDT-COF and Nafion on the surface of the Pt/C catalyst. Molecular dynamics simulations were further performed. The structures of Pt/C@Nafion and Pt/C@SDT-Nafion were built in a simplified model (Fig. 5, C and D; fig. S74; and table S6).

We calculated the radial density distributions for -SO₃H coordinating to Pt [$\rho_{\text{Pt-S}}(r)$] (Fig. 5E), and we compared the intensity of the first peak. The atom density profile of Pt-S decreased 0.6-fold after adding SDT-COF, which we attribute to the steric hindrance of SDT-COF. The height of the first peak of $\rho_{\text{Pt-O}}(r)$ increased 2.7-fold after the addition of SDT-COF (Fig. 5F), which revealed that more O₂ molecules can interact with the Pt catalyst. The simulation snapshots (figs. S75 and S76) showed that the ionomer chains took the chance to penetrate into mesopore apertures and interacted with the pore skeleton through hydrogen bond and van der Waals force, yet there remained apertures for water and oxygen molecules to pass through.

Conclusions

By introducing COFs, the MA, durability, and rate powder density can surpass and/or approach the DOE target (table S2) with unmodified commercial Pt/C, PtCo/C, or Pt/KB catalysts under low Pt loadings (0.07 mg_{Pt} cm⁻²). The DOE 2025 target is to reduce the Pt group metal total content to 0.1 g kW⁻¹ from the current level of 0.79 g kW⁻¹ (at 0.7 V). After using SDT-COF, the MEA with those commercial catalysts (0.32 g kW⁻¹ at 0.7 V and 0.16 g kW⁻¹ at 0.6 V) could approach this requirement. Moreover, the cost deduced from the whole CL is calculated to be \$19.5 per kilowatt, which can further reduce the cost of the conventional CL (~\$29 per kilowatt) by one-third. This strategy, together with the development of advanced catalysts, leads to efficient clean-energy storage opportunities. In addition, we used polystyrene sulfonic acid (PSA) to replace Nafion in the catalytic layer, and without further optimization, the performance of MEA by using the PSA-COF ionomer rivals the performance of pure Nafion (fig. S77). For the ionomer design principles, we introduced rigid network nanosheets with mesoporous apertures into the linear ionomer without sacrificing the proton conductivity. The thermal stability and structural designability of ionic COFs also make them promising in high-temperature fuel cells and alkaline fuel cells.

REFERENCES AND NOTES

1. L. Chong *et al.*, *Science* **362**, 1276–1281 (2018).
2. X. X. Wang, M. T. Swihart, G. Wu, *Nat. Catal.* **2**, 578–589 (2019).
3. C. Y. Ahn *et al.*, *Chem. Rev.* **121**, 15075–15140 (2021).
4. X. Tian *et al.*, *Science* **366**, 850–856 (2019).
5. A. Kusoglu, A. Z. Weber, *Chem. Rev.* **117**, 987–1104 (2017).
6. S. H. Kwon *et al.*, *Sci. Rep.* **11**, 8702 (2021).
7. S. Salari, M. Tam, C. McCague, J. Stumper, M. Bahrami, *J. Power Sources* **449**, 227479 (2020).
8. K. Shinozaki, Y. Morimoto, B. S. Pivovar, S. S. Kocha, *J. Power Sources* **325**, 745–751 (2016).
9. S. Ott *et al.*, *Nat. Mater.* **19**, 77–85 (2020).
10. Y. C. Park, H. Tokiwa, K. Kakinuma, M. Watanabe, M. Uchida, *J. Power Sources* **315**, 179–191 (2016).
11. V. Yarlagadda *et al.*, *ACS Energy Lett.* **3**, 618–621 (2018).
12. K. Kodama *et al.*, *ACS Catal.* **8**, 694–700 (2018).

13. K. Talukdar, P. Gazdzicki, K. A. Friedrich, *J. Power Sources* **439**, 227078 (2019).
14. S. So, H. Kang, D. Choi, K. H. Oh, *Int. J. Hydrogen Energy* **45**, 19891–19899 (2020).
15. H. Ren et al., *J. Power Sources* **506**, 230186 (2021).
16. S. Wang et al., *J. Power Sources* **379**, 338–343 (2018).
17. Z. Q. Tian, X. L. Wang, H. M. Zhang, B. L. Yi, S. P. Jiang, *Electrochem. Commun.* **8**, 1158–1162 (2006).
18. A. Fischer, J. Jindra, H. Wendt, *J. Appl. Electrochem.* **28**, 277–282 (1998).
19. K. Gu et al., *Mater. Today Energy* **19**, 100560 (2021).
20. E. Şengül, S. Erkan, I. Eroglu, N. Bac, *Chem. Eng. Commun.* **196**, 161–170 (2009).
21. S. Zhao et al., *Nat. Mater.* **20**, 1551–1558 (2021).
22. C. S. Diercks, O. M. Yaghi, *Science* **355**, eaal1585 (2017).
23. J. Li, S. Zhao, B. Wang, X. Feng, *Sci. China Chem.* **65**, 836–839 (2022).
24. Y. Yang et al., *Angew. Chem. Int. Ed.* **59**, 3678–3684 (2020).
25. L. Cao et al., *Adv. Mater.* **32**, e2005565 (2020).
26. S. Kandambeth et al., *Nat. Commun.* **6**, 6786 (2015).
27. X. Huang, C. Sun, X. Feng, *Sci. China Chem.* **63**, 1367–1390 (2020).
28. H. Liu et al., *Chem* **4**, 1696–1709 (2018).
29. S. J. Lyle et al., *J. Am. Chem. Soc.* **141**, 11253–11258 (2019).
30. A. Suzuki et al., *Int. J. Hydrogen Energy* **36**, 2221–2229 (2011).
31. M. R. Lee et al., *Fuel Cells (Weinh.)* **18**, 129–136 (2018).
32. The US DOE Fuel Cell Technologies Office (FCTO), Fuel cell technical team roadmap (DOE, 2017); https://www.energy.gov/sites/default/files/2017/11/t46/FCTT_Roadmap_Nov_2017_FINAL.pdf.
33. Y. V. Yakovlev et al., *J. Power Sources* **490**, 229531 (2021).
34. S. M. Alia, K. S. Reeves, J. S. Baxter, D. A. Cullen, *J. Electrochem. Soc.* **167**, 144512 (2020).
35. A. S. Rad, *J. Theor. App. Phys.* **10**, 307–313 (2016).

ACKNOWLEDGMENTS

This research was supported by the Analysis and Testing Center of the Beijing Institute of Technology for basic characterization. We thank G. Feng from Huazhong University of Science and Technology for his assistance in simulation calculations. We thank Y. Li, H. Wang, Y. Zhang, C. Hou, W. Zhang, W. Dong, C. Li, and L. Bao from Beijing Institute of Technology and J. Wang from Tsinghua University for their experimental assistance. **Funding:** This work was supported by the National Key Research and Development Program of China (2020YFB1506300); National Natural Science Foundation of China (grants no. 21922502, 22171022, 21805292, 21625102, and 21971017); Beijing Municipal Science and Technology Project (Z211100002421013); and China Postdoctoral Science Foundation (grants no. 2020T130055 and 2020M670143). **Author contributions:** Conceptualization: B.W.

and X.F.; Supervision: X.F. and B.W.; Methodology: X.F. and Q.Z.; Funding acquisition: X.F., Q.Z., and B.W.; Investigation: Q.Z., S.D., Y.Z., Z.M., P.S., D.S., X.J., T.Z., Z.R., J.X., and R.S.; Visualization: X.F., Q.Z., P.S., Y.Z., S.D., D.S., J.X., and R.S.; Writing – original draft: Q.Z., X.F., S.D., Z.M., and Y.Z.; Writing – review and editing: X.F., B.W., Q.Z., and P.S. **Competing interests:** B.W., X.F., and Q.Z. are inventors on patent application no. CN114361469A submitted by Beijing Institute of Technology, which covers COF-based porous ionomer for fuel cell. **Data and materials availability:** All data are available in the main text or the supplementary materials. **License information:** Copyright © 2022 the authors, some rights reserved; exclusive licensee American Association for the Advancement of Science. No claim to original US government works. <https://www.science.org/about/science-licenses-journal-article-reuse>

SUPPLEMENTARY MATERIALS

science.org/doi/10.1126/science.abm6304

Materials and Methods

Figs. S1 to S77

Tables S1 to S6

References (36–48)

Movies S1 and S2

Submitted 3 October 2021; resubmitted 26 April 2022

Accepted 26 August 2022

[10.1126/science.abm6304](https://doi.org/10.1126/science.abm6304)

Covalent organic framework–based porous ionomers for high-performance fuel cells

Qingnuan Zhang Shuda Dong Pengpeng Shao Yuhao Zhu Zhenjie Mu Dafei Sheng Teng Zhang Xin Jiang Ruiwen Shao Zhixin Ren Jing Xie Xiao Feng Bo Wang

Science, 378 (6616), • DOI: 10.1126/science.abm6304

Helping fuel cells breathe

In proton exchange membrane fuel cells, the Nafion ionomer usually overencapsulates and inhibits the platinum catalyst and can impede gas transport in the catalyst layer. Q. Zhang *et al.* showed that adding a sulfonated covalent organic framework (COF) to Nafion could improve the activity based on platinum by up to 60% (see the Perspective by Ma and Lutkenhaus). The hexagonal pores of the COF improve gas transport, and the sulfonic acid groups anchored on the pore walls decrease binding to platinum, which inhibits its activity. —PDS

View the article online

<https://www.science.org/doi/10.1126/science.abm6304>

Permissions

<https://www.science.org/help/reprints-and-permissions>

Use of this article is subject to the [Terms of service](#)

Science (ISSN) is published by the American Association for the Advancement of Science. 1200 New York Avenue NW, Washington, DC 20005. The title *Science* is a registered trademark of AAAS.

Copyright © 2022 The Authors, some rights reserved; exclusive licensee American Association for the Advancement of Science. No claim to original U.S. Government Works